Biomedical Microdevices (2022) 24: 36
https://doi.org/10.1007/s10544-022-00636-w

Digital filtering dissemination for optimizing impedance cytometry signal quality and counting accuracy

Brandon K. Ashley[1] · **Umer Hassan**[2]

Accepted: 4 October 2022 / Published online: 28 October 2022

Abstract

Improving biosensor performance which utilize impedance cytometry is a highly interested research topic for many clinical and diagnostic settings. During development, a sensor's design and external factors are rigorously optimized, but improvements in signal quality and interpretation are usually still necessary to produce a sensitive and accurate product. A common solution involves digital signal processing after sample analysis, but these methods frequently fall short in providing meaningful signal outcome changes. This shortcoming may arise from a lack of investigative research into selecting and using signal processing functions, as many choices in current sensors are based on either theoretical results or estimated hypotheses. While a ubiquitous condition set is improbable across diverse impedance cytometry designs, there lies a need for a streamlined and rapid analytical method for discovering those conditions for unique sensors. Herein, we present a comprehensive dissemination of digital filtering parameters applied on experimental impedance cytometry data for determining the limits of signal processing on signal quality improvements. Various filter orders, cutoff frequencies, and filter types are applied after data collection for highest achievable noise reduction. After designing and fabricating a microfluidic impedance cytometer, 9 μm polystyrene particles were measured under flow and signal quality improved by 6.09 dB when implementing digital filtering. This approached was then translated to isolated human neutrophils, where similarly, signal quality improved by 7.50 dB compared to its unfiltered original data. By sweeping all filtering conditions and devising a system to evaluate filtering performance both by signal quality and object counting accuracy, this may serve as a framework for future systems to determine their appropriately optimized filtering configuration.

Keywords Impedance Cytometry · Microfluidics · Signal Processing · Leukocyte counting

1 Introduction

Highly sensitive and accurate biosensors are continuously researched and sought out to measure critical and often microscopic analytes, providing decisive and time-dependent information in biological systems. This imperative form is used in diverse settings, from critical care disease diagnostics (Ashley and Hassan 2021a; Murdock et al. 2017; Lu et al. 2015b; Zhang et al. 2020), continuous and discrete physiological monitoring (Ashley et al. 2019; Brown et al. 2018; Gao et al. 2016; Koh et al. 2016), environmental monitoring (Alam et al. 2020; Lu et al. 2015a; Marinov et al. 2018), and manufacturing/product development quality control (Cinti et al. 2017; Izadi et al. 2016; Verma and Singh 2003). The assorted materials and compounds to measure additionally prompts a variety of detection modalities in which to measure them, each with their advantages in specific conditions. This includes modalities such as fluorescence microscopy (Hu et al. 2014; Maetzig et al. 2017; Volpetti et al. 2015), acoustic imaging (Gnyawali et al. 2019; Khateib et al. 2020; Sarimollaoglu et al. 2014), surface plasmon resonance (Sun et al. 2020; Yoo et al. 2020), and biochemical assays (Cho and Irudayaraj 2013; Han et al. 2007). Among the vast technologies, electrochemical impedance spectroscopy (EIS) stands out as a versatile, accurate, and rapid technique and has demonstrated minimal reagent preparation, miniscule sample volumes, and non-destructive sample measurement for a variety of materials (Bredar et al. 2020; Hassan et al. 2017; Lu et al. 2015b; Stupin et al. 2017). In a subsection of

✉ Umer Hassan
umer.hassan@rutgers.edu

[1] Department of Biomedical Engineering, Rutgers, the State University of New Jersey, Piscataway, NJ 08854, USA

[2] Department of Electrical Engineering, Department of Biomedical Engineering, and Global Health Institute Rutgers, the State University of New Jersey, Piscataway, NJ 08854, USA

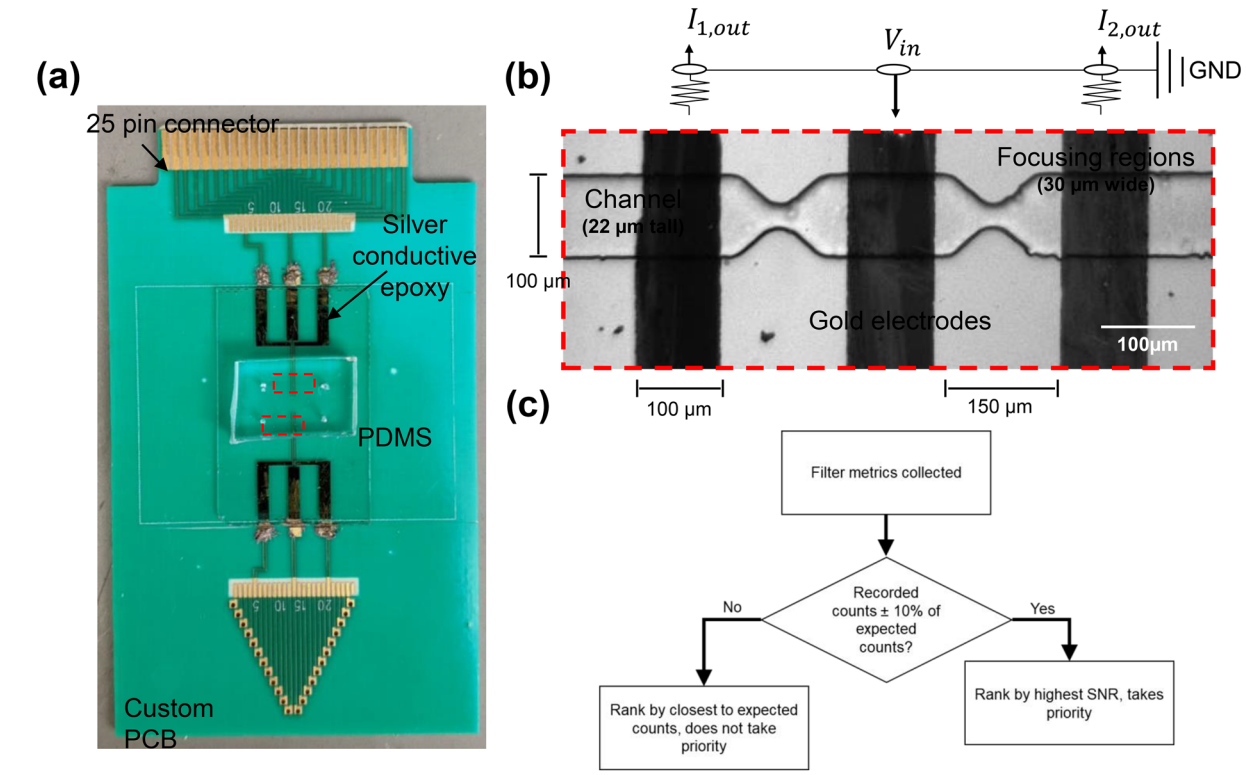
(a)
25 pin connector
Silver conductive epoxy
PDMS
Custom PCB
(b)
$I_{1,out}$
V_{in}
$I_{2,out}$
GND
Focusing regions (30 µm wide)
Channel (22 µm tall)
100 µm
Gold electrodes
100µm
100 µm
150 µm
(c)
Filter metrics collected
Recorded counts ± 10% of expected counts?
No
Yes
Rank by closest to expected counts, does not take priority
Rank by highest SNR, takes priority

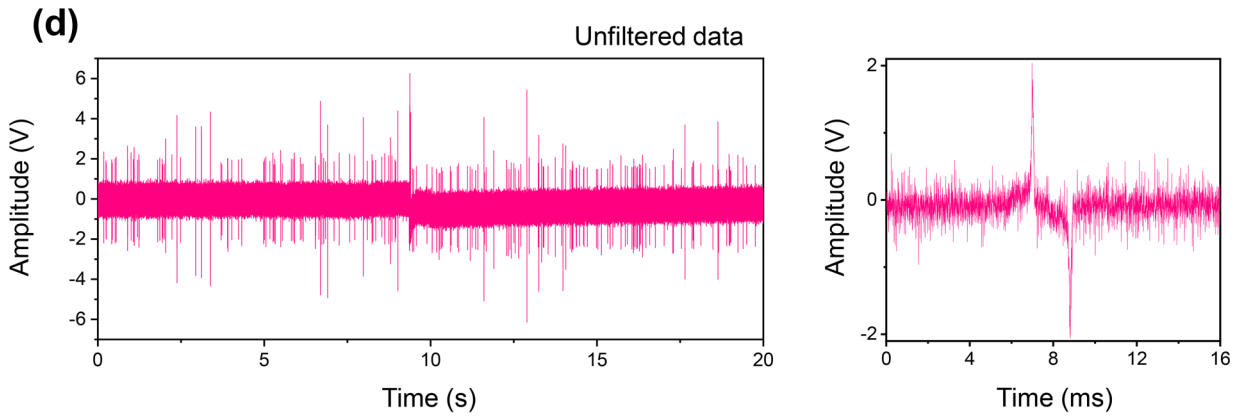
(d)
Unfiltered data
Amplitude (V)
Time (s)
Time (ms)

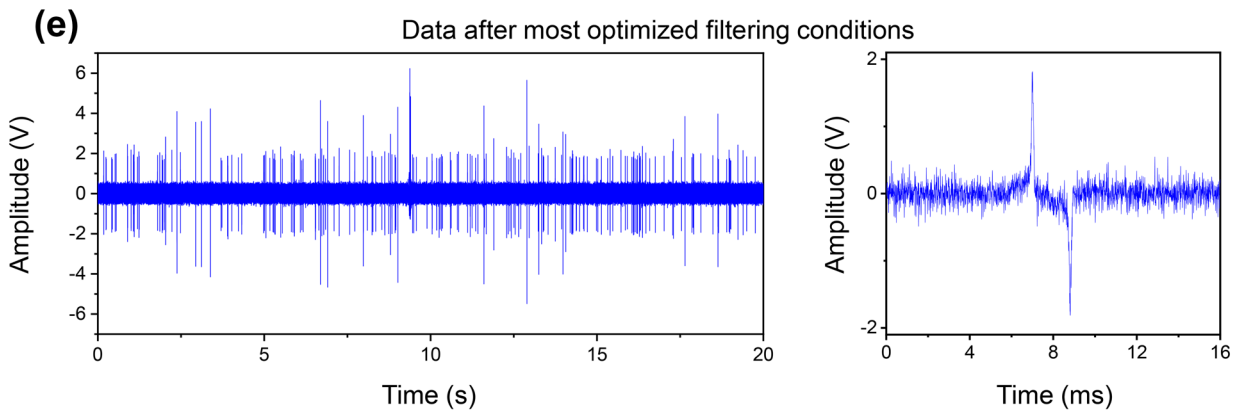
(e)
Data after most optimized filtering conditions
Amplitude (V)
Time (s)
Time (ms)

◂**Fig. 1** **a** Custom printed circuit board (PCB) which onboards microfabricated microfluidic impedance cytometry device. Silver conductive epoxy adheres and facilitates electron transfer between gold microelectrodes and computer-connector interface. **b** Brightfield microscope image of microfluidic electric field regime. A polydimethylsiloxane (PDMS)-based channel has focusing regions between gold electrodes which increases particle pulse amplitude. The middle electrode is voltage stimulated (V_{in}) and exterior detecting electrodes produces an electric field in the region. **c** Flowchart of digital filtering selection criteria and how filtering conditions were ranked for signal quality optimization. **d** Time-domain impedance detection data of 9-micron polystyrene particles collected from the microfluidic device prior to applying digital filtering. A differential signal is collected from the two detecting electrodes, followed by transimpedance current amplification which produces a bipolar pulse for each particle. **e** The same impedance data after digital filtering with the most optimized conditions (1^{st} order Butterworth low pass filter at a 60 kHz cutoff frequency and 3^{rd} order Chebyshev Type I high pass filter at a 30 Hz cutoff frequency) which reveals lower noise band and baseline drift per polystyrene pulse signal amplitude

EIS, microfluidic impedance cytometry is the recordings of microscopic materials flowing through a microfluidic channel and disrupting a defined electric field, and has been used extensively for its manufacturing ease and simple data processing in point-of-care settings (Ashley and Hassan 2021b; Clausen et al. 2018; Colson and Michel 2021; Zhong et al. 2021).

Unfortunately, each of these choices comes with their own competitive unvalued noise sources which impedes the intended analyte's detection. For EIS, this originates from interferences such as surrounding electrical generation, sample volume electrical properties, external ionization, and sample collection quantization (Antal et al. 2001; Pierce et al. 2015; Ram et al. 2012). Perfecting experimental conditions may reduce noise from these sources, but in many fields these conditions are uncontrollable and may not reduce noise to a sufficient degree (Ridgway et al. 2007).

Without alternatives, a capable approach is processing post-data collection, where property differences between signal and noise data may be exploited (Hassan et al. 2015). Transforming the data into frequency space reveals this exploitation, where specific frequency regimes are notorious for predominate noise. This includes low frequencies typically below 30 Hz, where high amplitude, low frequency noise manifests into data drift over time, corrupting the detection range and primarily disrupting accurate desired signal recognition (Atakan et al. 1980; Chouhan and Mehta 2007; Liu et al. 2014; Sun et al. 2007). Contrastingly, high frequencies above 100 kHz also constitute majority noise results, as frequency data from material recordings generally fall within 0.03 to 100 kHz (Ashley and Hassan 2021c; Hassan et al. 2015). This high frequency noise produces a wide noise band in the data, where signal identities close to a device' detection limit may fall underneath and become degraded (Ashley and Hassan 2021b). While these are the general values, in practice the specific frequencies which represent analyte data has not been fully explored, being only defined from theoretical hypotheses (Antal et al. 2001; Stupin et al. 2017). There lies a need for understanding and experimental justification for specific frequency filtering which may improve sensor data signal quality and accuracy.

Often, digital filtering is used with many detection modalities, including EIS (Hassan et al. 2015; Manikandan and Soman 2012; Ram et al. 2012; Redhyka et al. 2015). However, when critical materials must be measured near the technology's detection limit, the smallest of margins and signal quality optimizations may correspond to significant detection accuracy improvements. While applied, there is inadequate research on experimental impedance cytometry data related to which digital filtering conditions have the highest performance. Therefore, this article aims to execute a library of digital filtering conditions and provide a structure for defining signal quality in impedance cytometry data. Polystyrene particles 9 μm in diameter are measured through a microfabricated, microfluidic impedance cytometer (Fig. 1a, b). As shown by Fig. 1c, when assessing filtering performance, emphasis will be placed on counting accuracy first, followed by higher signal-to-noise ratios (SNR) related to higher signal quality. After transimpedance amplification, a litany of filter types, filter orders, and cutoff frequencies will be assessed in transforming the original unfiltered result (Fig. 1d) to its defined, most optimized form (Fig. 1e). This approach will further be presented with biologically relevant samples of isolated human neutrophils to support its formulation. While systematically defined, this article is the first to explore digital filtering variations in experimental EIS data and provide guidance on future and more diverse filtering selections.

2 Materials and methods

2.1 Materials

Phosphate buffered saline (PBS, 1X and 10X), Ficoll-Paque density gradient, (3-Amino-propyl)triethoxysilane (APTES), and Roswell Park Memorial Institute medium 1640 (RPMI) were purchased through Sigma Aldrich (St. Louis, MO, USA). A NE-300 syringe pump was purchased from Southpoint Surgical Supply (Coral Springs, FL, USA). A HF2LI lock-in amplifier and HF2TA current amplifier was purchased through Zurich Instruments (Zurich, SUI). Silver conductive epoxy was purchased from Digi-Key (Thief River Falls, MN, USA). Unidentifiable human blood was obtained from Robert Wood Johnson Medical Hospital (New Brunswick, NJ, USA) through an institutional review board (IRB) study. LabView software was purchased and installed through National Instruments (Austin, TX, USA). MATLAB

version 2020B was purchased and installed through Mathworks (Natick, MA, USA).

2.2 Microelectrode and microchannel fabrication

Gold-electrodes are microfabricated on borosilicate glass wafers above a deposited chromium adhesion layer following the manufacturers protocol for s1813 photolithography. Microfluidic channel molds are also microfabricated on silicon wafers following the manufacturers protocol for SU-8 3025 photolithography. Polydimethylsiloxane (PDMS) is poured and cured over SU-8 channel molds, and after removal a biopsy punch creates inlet and outlet holes to facilitate media perfusion from syringe tubing and a syringe pump. PDMS and gold electrode surfaces are treated with oxygen plasma and bonded, where focusing regions are aligned across electrodes to increase polystyrene particle volume fraction in the electric field space. Key channel dimensions include 100 µm in width, with focusing regions reducing the width to 30 µm, 22 µm in height, and is 3 cm long. Microelectrodes are 0.5 µm thick, are 100 µm in width, and are 150 µm apart (Fig. 1b) (Holmes et al. 2006). More specific microfabrication procedures with this configuration have been previously published, and further detail is included in the Supplemental Information (Ashley et al. 2021; Ashley and Hassan 2021b).

2.3 Signal acquisition, demodulation, and data processing

Silver conductive epoxy adheres gold electrodes to a custom printed circuit board using electrode contact pads, visualized in Fig. 1a. A 5 V AC input is applied to the center electrode using the HF2LI signal amplifier, and the HF2TA current amplifier increase recorded signal contributions from the device. 9 µm polystyrene microparticles are diluted in phosphate buffered saline at a 35 particle/µL concentration and undergo flow at a rate of 15 µL/min. The signal is recorded at a 250 kHz sampling rate using a PCIe-6361 data acquisition card, and dual detecting (grounded) electrode recordings are subtracted to produce a bipolar impedance pulse.

Impedance cytometry recordings are saved through a LabView control program and interpreted in a custom MATLAB script. A region manually selected which is absent of particles is used as the noise reference values, which is the standard deviation of the selected region. A threshold is then applied for the absolute value of data 4 times this noise standard deviation to define the particle pulse, construing the data as 9 µm polystyrene microparticles. If the average of the threshold triggering data point and the next 10 data points is less than the threshold, the pulse is neglected, which removes high frequency noise data that may have triggered a false positive hit above the threshold. Additionally, after collecting all the particle pulses and obtaining their average peak-to-peak amplitudes, pulses which are 2 times greater than average are neglected, as these represent two or more particles traveling across the electric field regime simultaneously. For this study, we are only interested in evaluating the signal quality for individual 9 µm polystyrene microparticles, as more than one particle disrupting the electric field at once may artificially inflate the average signal quality of the sample. More detail on instrumentation and microfluidic channel framework may be found in the Supplemental Information (SI Fig. 1).

2.4 Applying and evaluating digital filtering

Using MATLAB, when a data value goes beyond the defined threshold, the magnitudes of the highest and lowest values of the next 500 data points are combined to produce the peak-to-peak bipolar amplitude (ΔV_T) for an individual particle:

$$\Delta V_T = \Delta Vmax - \Delta Vmin \tag{1}$$

Following this, the standard deviation of the previous 200 data points is measured which defines the local noise prior to particle pulse detection:

$$\sigma_{BG} = \sqrt{\frac{1}{n}\sum\nolimits_i x_i^2} \tag{2}$$

The signal-to-noise ratio for each particle is then quantified as the logarithm ratio of bipolar amplitude with data standard deviation prior to pulse detection, standardized to a decibel scale:

$$SNR = 20\log\frac{\Delta V_T}{\sigma_{BG}} \tag{3}$$

For a 60 s recording segment and from the expected diluted concentration of 35 particles/µL which flows through the channel at 15 µL/min, the expected particle count is approximately 525 particles. Accounting for a 10% error given micro-changes in concentration under flow, different filtering conditions described next are rated by increasing SNR if the counted number of particles is within this 10% error range (Fig. 1c). If the recorded particle counts deviate 10% away from the 525-particle count average, filter conditions are rated by the closest counts to expected, as these conditions are rated less favorably since many false positive or false negative measurements occur, indicating an unoptimized system. Future experiments are underway with simultaneous high speed video microscopy to capture true object incidence, which can reduce the % error range for defining counting accuracy.

The original unfiltered data is shown in Fig. 1d, with examples of baseline drift represented along with an apparent noise band. Dual detecting electrode recordings are subtracted to produce a bipolar impedance pulse shown by the zoomed-in insert. Butterworth, Chebyshev Type I (Cheby1), and Chebyshev Type II (Cheby2) digital filters are applied in MATLAB for both high pass and low pass filtering conditions. Both Cheby1 and Cheby2 filters are operating with a 5 dB ripple for the passband (Cheby1) or stopband (Cheby2). For each experiment, powerline interference filtering is also applied with 4^{th} order band-stop filters at 60 Hz and its 120 Hz second harmonic. Figure 1e represents the most optimized filtering conditions achieved with this approach of the 9 µm polystyrene particle samples, revealing a smaller noise-band and removed baseline drift, and will be determined and discussed in the following sections. Data Fourier transformations is performed in MATLAB using the Fast Fourier Transform or fft command.

From previous reports, particle pulse data collected from micro flowing impedance cytometry lies between 50 Hz and 90 kHz when flowing at an approximate 15 µL/min rate (Hassan et al. 2015). Therefore, a significant majority of amplitudes above 90 kHz is contributed from high frequency noise and produces the large time-domain noise band. It is expected that eliminating frequencies near or above this 90 kHz value may reduce this band and improve signal quality without significantly reducing desired object pulse data. Thus, for cutoff frequency selection for digital filtering in the subsequent sections, cutoff frequencies are varied from 5 to 50 Hz at different filter orders with a 5 Hz step for high pass filtering. Cutoff frequencies are varied from 60 to 125 kHz with a 15 kHz with low pass filtering. Along with filter types, filter orders for each type with each filtering pass are modulated from 1^{st} to 4^{th} order and disseminated to determine the highest achievable SNR with measured particle counts close to expected particle counts.

2.5 Isolating neutrophils from whole blood

Deidentified whole blood was obtained from patient samples and Robert Wood Johnson University Hospital through an IRB study (Wagner et al. 2021). After collection, blood was combined with 1X PBS at equal volumes, and layered above Ficoll-Paque density gradient at a 3 to 4 ratio. This amalgam is centrifuged for 30 min at 400 g which exploits density differences to separate platelets, blood cells, and plasma. Platelets and plasma are aspirated in the supernatant, with the blood cell pellet exposed to deionized water for 15 s to dissolve non-neutrophil mononuclear cells. Tonicity was rebalanced with 10X PBS, and the solution was again centrifuged for 5 min at 300 g to separate red blood cells from neutrophils. This process is repeated until a gray pellet appears, representing isolated neutrophils, and this pellet was resuspended in RPMI 1640 media with 50 µL of stock neutrophils to 5 mL of RPMI 1640 media. Immediately prior to impedance cytometry experiments, neutrophils are diluted in 1X PBS.

3 Results and discussion

3.1 Data Fourier transformation to determine filtering ranges

Figure 2 outlines the Fourier transform (Fig. 2b, c) of the entire unfiltered data (Fig. 2a), highlighting specific regimes which contain significant noise contributions which are evaluated in this report, including low frequency noise (Fig. 2d) and high frequency noise (Fig. 2e). The goal with cutoff frequency selections is to produce the highest noise elimination without additionally eliminated frequency data from particle pulses. Visualized by Fig. 2d, baseline drift is a large frequency amplitude contribution below 5 Hz which arises from external ionization of surrounding electrical devices and micro-variances in microfluidic flow (Pierce et al. 2015). These observations affirm the cutoff frequencies used for both high and low frequency noise filtering for the following sections to improve signal quality and accuracy.

3.2 Impact of high pass filtering on signal quality

As mentioned previously, eliminating low frequency noise reduces baseline drift effects, and predicted to increase object counting accuracy and modestly decrease the noise amplitude (Atakan et al. 1980; Liu et al. 2014). When assessing measurement performance for biosensors including this impedance cytometry device, the most important metrics include high SNRs and accurate object determination. Regarding these experiments, SNR is closely tied to the bulk noise amplitude, while accurate object counting is related to the expected object concentration in the sample. Therefore, the number of particles measured in a constant time measurement, the samples noise amplitude, and the composite SNR will define the improvements in signal quality brought about by the digital filtering conditions. When no digital filtering is applied, the referenced sample metrics includes a 0.2468 V noise amplitude, a 20.54 dB SNR, and counted 971 particles which is significantly inaccurate to the expected 525 particle counting concentration.

Figure 3 details the noise, SNR, and number of 9 µm polystyrene particles counted in the same sample data with a myriad of high pass digital filtering conditions used without other simultaneous digital filtering. What remains consistent across filter types is a higher likelihood of reduced counting accuracy at higher cutoff frequencies (see filter orders 1 and 2 in Fig. 3a, filter order 2 in Fig. 3d, and filter

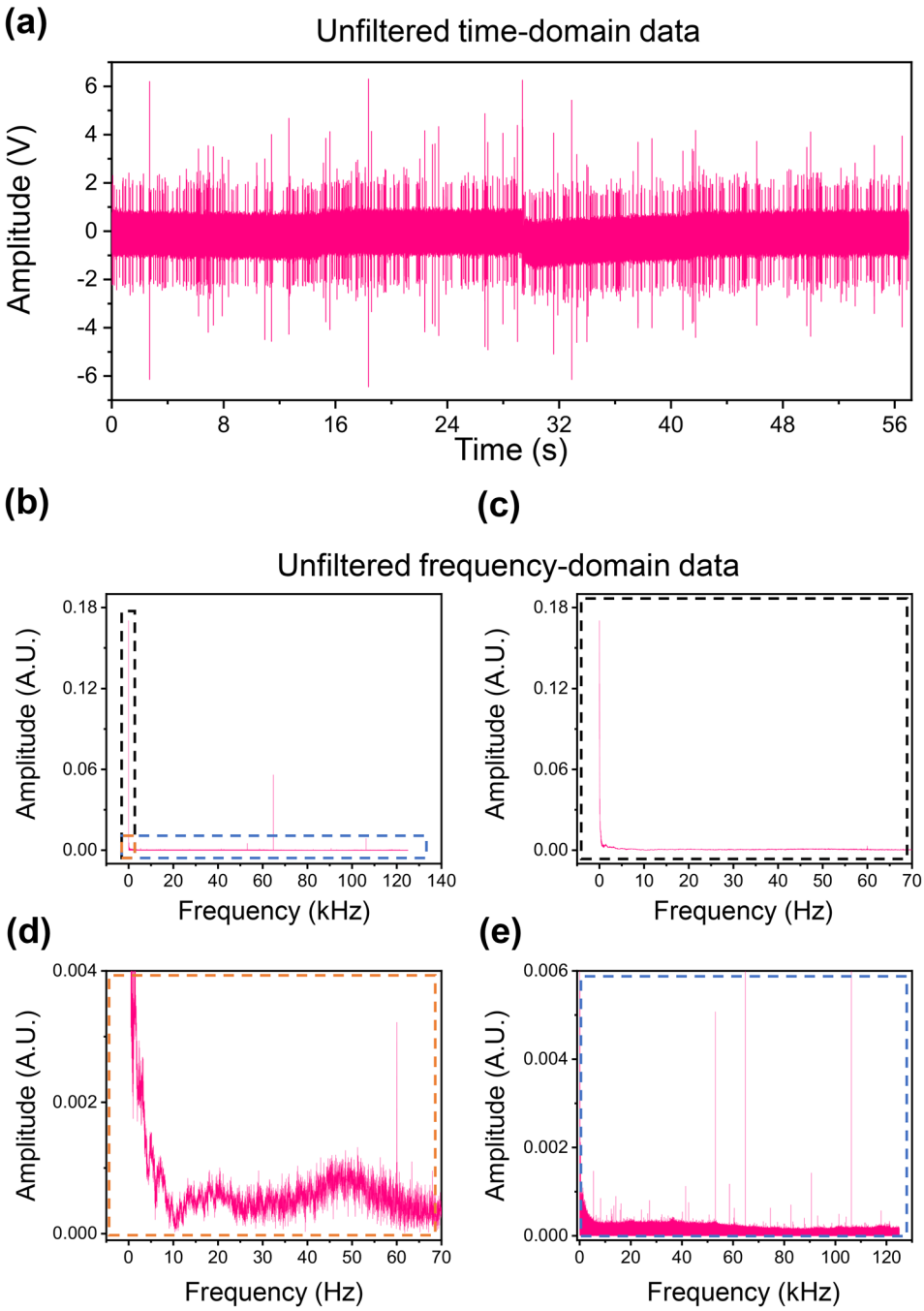

Fig. 2 **a** Full time-domain recording data of unfiltered 9 micron polystyrene impedance pulses. **b** Full Fourier transformation of recordings with highlighted high-noise frequency regimes: low noise amplitude (**c**), powerline interference (**d**), and high frequency noise above approximately 90 kHz (**e**)

orders 1 and 3 in Fig. 3g). This sharp rise in false positive counts results from removing particle pulse frequency data in this low frequency regime and producing a thresholding value less likely to discern pulse data from high amplitude noise data. As a result, inaccurate and over-counting trickles down to impact average samples noise amplitude, and with a reduced average bipolar pulse amplitude measured that includes lower false positive noise amplitude, the SNR is lower relative to other conditions (see filter orders 1 and 2 in Fig. 3c, filter order 2 in Fig. 3f, and filter orders 1 and 3 in Fig. 3i). It would be expected then that the most optimal cutoff frequency across the filters would be the highest value that does not trigger an inaccurate count and thereby eliminating baseline drift noise to its fullest degree. Otherwise, there are no significant trends between filter orders which dictate filtering roll-off steepness, while Cheby1 filters have a marginally higher average SNR than Butterworth or Cheby2 filters at the same cutoff frequency and filter order.

Using the ranking system outlined in Fig. 1c, each filter order, cutoff frequency, and filter type iteration was arranged

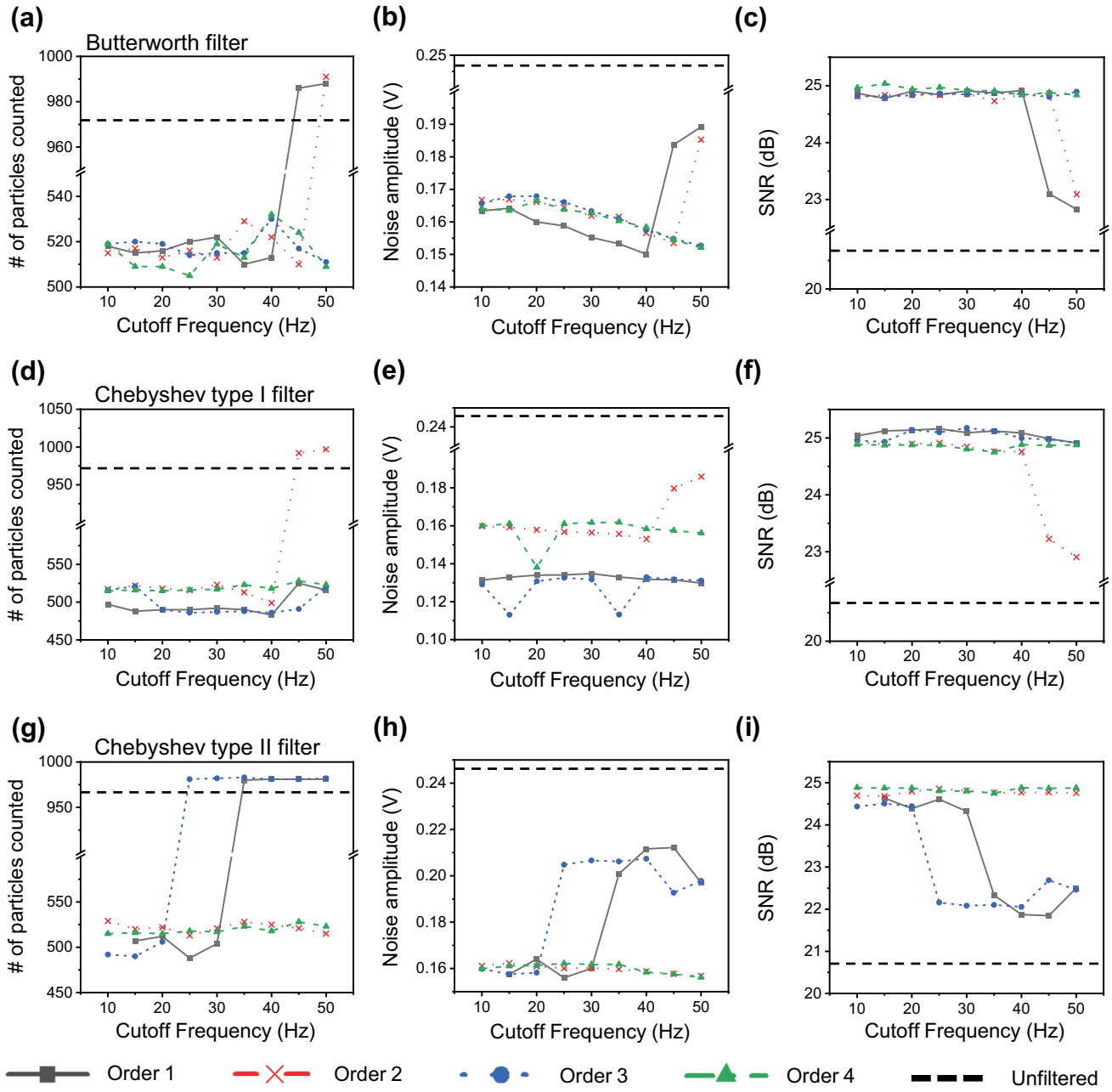

Fig. 3 High pass filtering results alone when varying the cutoff frequency (10 Hz to 50 Hz) with different filter types (Butterworth (**a**-**c**), Chebyshev Type I (**d**-**f**), Chebyshev Type II (**g**-**i**) filter types) and different filter orders: 1st order (gray), 2nd order (red), 3rd order (blue), 4th order (green). Results compared with the number of particles counted through the impedance detection recording (**a**, **d**, **g**), the average background noise (**b**, **e**, **h**), and the SNR or signal to noise ratio (**c**, **f**, **i**) across the different filter types, orders, and cutoff frequencies. Black dotted lines represent unfiltered values for comparison

in a hierarchy from most to least optimized to improve signal quality (Table 1 and SI Table 1). Based on noise reduction, relative SNR increases, and counting particles within a 10% margin of error to the expected counts, the high pass filtering alone which improved signal quality the most was the 3rd order Cheby1 filter with a 30 Hz cutoff frequency. This aligns with our expected midpoint cutoff frequency value between 5 and 50 Hz, delivering the highest SNR of the over 100 different filter parameter combinations (SI Table 1). The highest performing Butterworth filter was ranked 11th, which was a 3rd order filter with a 15 Hz cutoff frequency, while the highest performing Cheby2 filter was ranked 39th with a 4th order filter at 10 Hz. Of note, Cheby1 filters typically outperformed Butterworth and Cheby2 filters with similar conditions, and were less likely to experience the inaccurate counting issue as Cheby2 filters made up 10 of

Table 1 Highest ranking high pass alone filtering conditions for each filter type

Filter type, order, and cutoff frequency	# of particles counted	Noise (V)	SNR (dB)	Overall rank
Cheby1, 3rd order, 30 Hz	487	0.1317	25.1761	1
Butterworth, 3rd order, 15 Hz	520	0.1679	25.0369	11
Cheby2, 4th order, 10 Hz	515	0.1599	24.8857	39

the 15 configurations which counted particles outside of the 10% margin of error (SI Table 1). Otherwise, there were no apparent trends related to filter order throughout the ranks.

3.3 Impact of low pass filtering and the most optimized high pass filtering on signal quality

While high-pass filtering primarily eliminates baseline drift, low-pass filtering is expected to greater reduce the noise band and increase SNR. When evaluating signal quality alone, however, the lack of baseline drift negation heavily impairs the counting accuracy and signal quality achieved from even the most optimized low pass filtering conditions (SI Fig. 2). As such, the next results will focus primarily on modulating low-pass filtering conditions in conjunction with the most optimized high-pass filtering parameters achieved in the previous Sect. (3rd order Cheby1 filter with 30 Hz cutoff frequency).

In evaluating low-pass filtering effects, Fig. 4 presents trends with cutoff frequency across different filter orders and filter types. Similar to Fig. 3, the graphs are presented as the key metrics in determining signal quality; the number of counted particles, average background noise amplitude, and SNR. Other than 2 iterations with the 4th order Cheby1 filter below 75 kHz, all configurations were within 10% of the counting error and had adequate counting accuracy. Unlike the high-pass alone conditions, there is a trend with cutoff frequency and SNR/noise amplitude, as across the filters and orders a lower cutoff frequency corresponded with a lower noise amplitude and higher SNR. This is consistent with the ranked filtering conditions (Table 2), as each filter type's highest rank was with a 60 kHz cutoff frequency. For these parameters, the highest rank overall used a 1st order Butterworth filter, while the highest Cheby1 filter was ranked 4th and Cheby2 filter ranked 7th. Contrasting to the high-pass filtering results alone, there is an even distribution of filter types in the top ranks of low-pass filtering signal quality (SI Table 2). However, filter order results did not have consistent relationships to filter type, as cutoff frequency dominated the correlation with signal quality ranks. With this combinatorial filtering, SNR increased 6.09 dB and placed the device within an acceptable counting range compared to the unfiltered data.

It was previously believed that frequencies below 90 kHz for this device's configuration also included considerable desired signal components, and therefore cutoff frequencies for a low pass filter below 90 kHz would decrease signal quality relative to a higher cutoff frequency (Hassan et al. 2015). However, the results presented here reflects a greater noise reduction offset down to 60 kHz, even as particle bipolar amplitude slightly declines as well (Fig. 1d). This proves the power noise reduction has on SNR relative to the measured signal amplitude, and future directions may research filtering conditions which go below this 60 kHz low pass cutoff frequency as well to determine optimal signal quality.

In both high-pass and low-pass filtering analysis, the Cheby1 filter generally outperformed the Butterworth and Cheby2 filters in noise reduction at identical filter order and cutoff frequency conditions. This is expected, as ideal Cheby1 filters have a larger stopband attenuation magnitude farther halfway through the stopband frequency range compared to a Butterworth filter with the same cutoff frequency and filter order (Taylor and Williams 2006; Weinberg and Slepian 1960). Additionally, the Cheby2 filter performed the worst in attenuating baseline drift, most likely due to the ripple in the stopband inhibiting greater noise reduction as opposed to the ripple being in the passband for Cheby1 filters (Bianchi and Sorrentino 2007; Singh et al. 2010). The severity of this effect in the low-pass results was not as apparent, as the stopband at lower cutoff frequencies also included polystyrene particle pulse data. One consideration may be computational time for applying digital filters, as for identical conditions Butterworth filters have a faster step response (Singh et al. 2010). However, for the reported analysis, additional time for digital filtering did not exceed 3 s for any experimental condition, including combinatorial high-pass and low-pass experiments. When optimal filtering conditions are determined and real-time filtering is applied to future experiments, computer memory buffers settings may be applied to discretize smaller data sections and accommodate for the required filter computing time.

3.4 Applying filtering conditions to isolated neutrophil data

To evaluate the procedural robustness of optimizing digital filtering conditions for time-domain impedance cytometry data, this approach was translated to more heterogenous samples with greater biomedical applications. Specifically, isolated neutrophils from human whole blood were

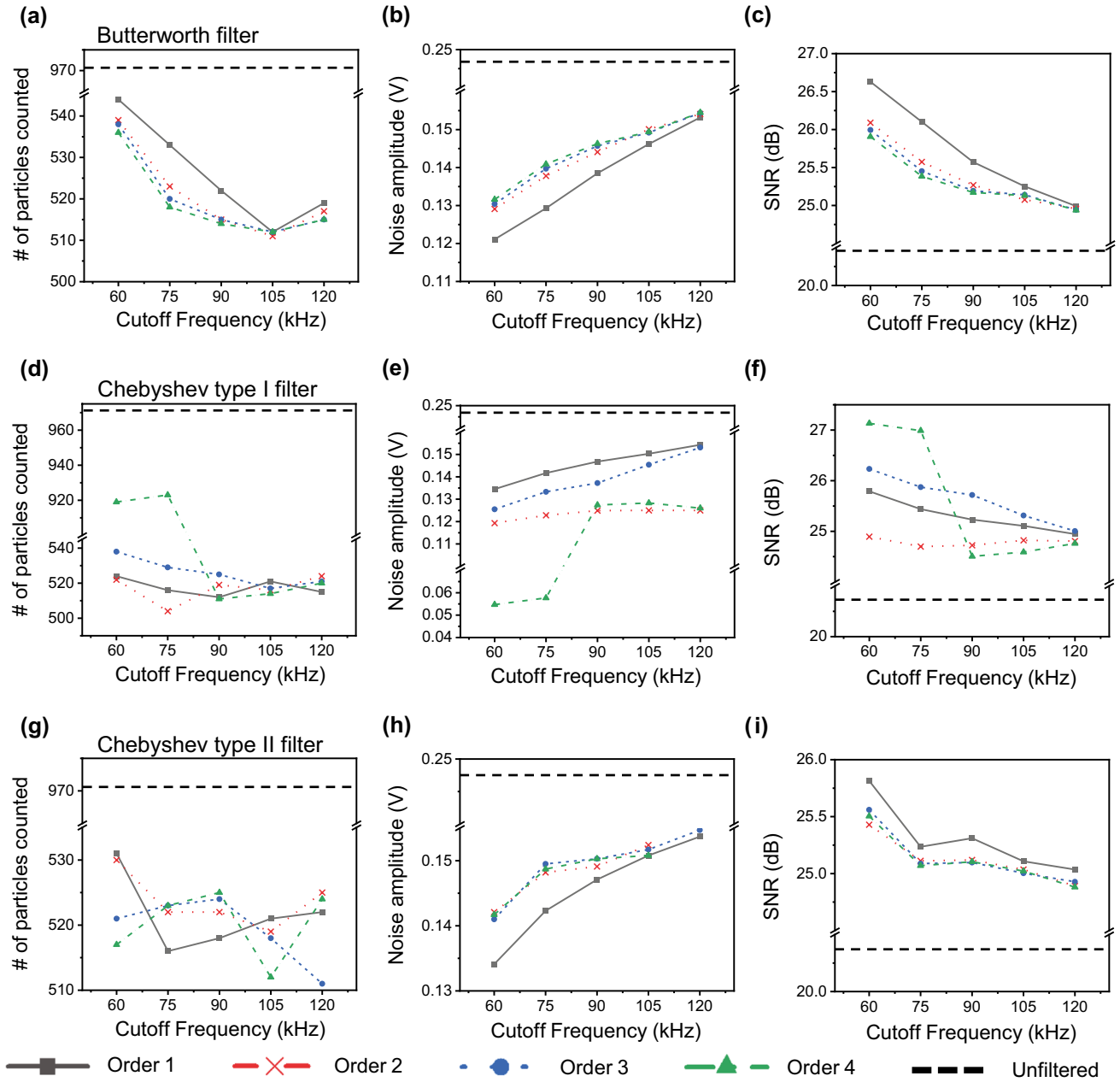

Fig. 4 Low pass filtering results when varying the cutoff frequency (60 kHz to 120 kHz) with different filter types (Butterworth (**a**-**c**), Chebyshev Type I (**d**-**f**), Chebyshev Type II (**g**-**i**) filter types) and different filter orders: 1st order (gray), 2nd order (red), 3rd order (blue), 4th order (green). Results compared with the number of particles counted through the impedance detection recording (**a**, **d**, **g**), the average background noise (**b**, **e**, **h**), and the SNR or signal to noise ratio (**c**, **f**, **i**) across the different filter types, orders, and cutoff frequencies. Statistics presented also simultaneously include filtering with the most optimized high pass filtering results (Cheby1, 3rd order, 30 Hz). Black dotted lines represent unfiltered values for comparison

Table 2 Highest ranking low pass alone filtering conditions for each filter type including the highest ranking high pass filtering conditions (Cheby1, 3rd order, 30 Hz)

Filter type, order, and cutoff frequency	# of particles counted	Noise (V)	SNR (dB)	Overall rank
Butterworth, 1st order, 60 kHz	544	0.1211	26.6293	1
Cheby1, 3rd order, 60 kHz	538	0.1255	26.2322	4
Cheby2, 2nd order, 60 kHz	530	0.1421	25.4292	7

measured in the designed microfluidic impedance cytometer, and the same iterative process was used to determine the low and high pass digital filtering conditions that generated the highest SNR while also remaining within ± %10 of the expected number of neutrophils counted across the sample recording. Here, neutrophils were diluted to 5×10^4 cells/mL, and over a 60 s recording with the same 15 µL/min the expected number of cells to count was 750.

Figure 5 represents the time-domain impedance data of counted neutrophils measured with the microfluidic impedance cytometer before (Fig. 5a) and after (Fig. 5b) digital filtering was applied. Here, there is a more apparent baseline drift consideration, although this did not greatly impact the neutrophil counting results the number of counted cells at 769 was still within ± %10 of the expected 750 count. Additionally, only a select number of filters were evaluated based on filter conditions from this group's previous publications as well as the highest-performing filter conditions from the previous sections in this article (Ashley and Hassan 2021b; Hassan et al. 2015). It is notable that our previous digital filtering conditions delivered the lowest increase in SNR (4^{th} order Butterworth high pass filter with a 20 Hz cutoff, 4^{th} order Butterworth low pass filter with a 120 kHz cutoff), and changes in filter cutoff frequencies appeared to have most significant SNR impacts.

Many—but not all—trends remain consistent to the 9 µm polystyrene test particle results. This includes lower low-pass filtering cutoff frequencies between 60 to 75 kHz delivered higher SNRs, the 25–30 Hz cutoff frequency range for high-pass filtering was optimal to remove baseline drift without greatly disrupting neutrophil signal quality, and the Cheby1 filters were found higher ranking than Butterworth or Cheby2 filters (Table 3). However, the most optimal filtering conditions for the neutrophil data was not identical to the previous section results: here, the most optimal filtering conditions were a 3^{rd} order Cheby1 high-pass filter with a 30 Hz cutoff and a 3^{rd} order Cheby1 low-pass filter with a 60 kHz cutoff, while the filtering

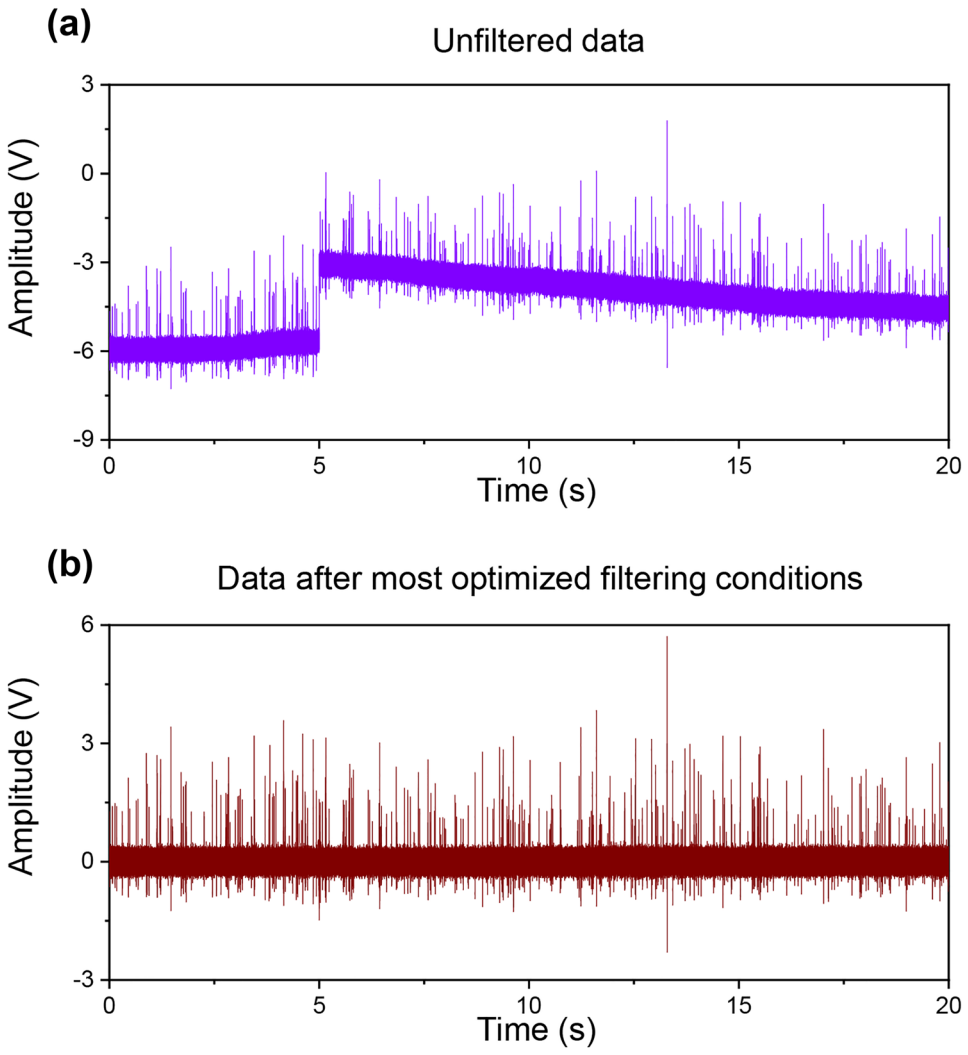

Fig. 5 Time domain-data with isolated neutrophil impedance pulses before (**a**) and after (**b**) optimized digital signal filtering (3^{rd} order Chebyshev Type I high pass filter at a 30 Hz cutoff frequency and $3.^{rd}$ order Chebyshev Type I low pass filter at a 60 kHz cutoff frequency)

Table 3 Highest ranking low and high pass filtering conditions for isolated human neutrophil impedance data

Filter type, order, and cutoff frequency	# of particles counted	Noise (V)	SNR (dB)	Overall rank
High pass: Cheby1, 3rd order, 30 Hz Low pass: Cheby1, 3rd order, 60 kHz	716	0.1425	26.6806	1
High pass: Cheby1, 3rd order, 30 Hz Low pass: Cheby1, 4th order, 75 kHz	726	0.1320	26.6108	2
High pass: Cheby1, 3rd order, 30 Hz Low pass: Butterworth, 1st order, 60 kHz	719	0.1425	26.5687	3
High pass: Cheby1, 1st order, 25 Hz Low pass: Butterworth, 1st order, 60 kHz	724	0.1455	26.4198	4
High pass: Butterworth, 4th order, 20 Hz Low pass: Butterworth, 4th order, 120 kHz	726	0.1515	26.4095	5
Unfiltered	769	0.1770	19.1833	6

conditions most optimal for the 9 μm polystyrene test particle results ranked 3rd in signal quality for the neutrophil data. This most likely arises from the small margins which separate all these conditions, as only a 0.11 dB change in SNR exists between these two conditions, so the smallest impacts in bipolar amplitude frequency data between neutrophils and polystyrene particles, flow perturbations, or local media conductivity may change the final numerical result. Nonetheless, the aim of these results is to highlight the methodology for determining the most optimal filtering conditions and which signal quality metrics contribute to those decisions.

It has been demonstrated that a lack of experimental analysis produced sub-ideal signal processing, and the framework put forth in this article can provide clarity for other systems to find their own signal processing best fits. This digital filtering approach may be used with minimal modulation, including for systems of varying experimental or instrumental forms, such as different channel dimensions, different electric field magnitudes, or using single-ended measurements. While exhaustive filtering conditions were highlighted, future applications of this method can omit some steps like including Cheby2 filters or extreme cutoff frequency ranges to evaluate filtering results more efficiently. Collecting the highest feasible signal quality in a biomedical device is greatly important for measuring minute but critical analyte changes and lowering a systems detection limit, which in turn can increase the sensitivity and accuracy of these highly depended-upon machines.

Supplementary Information The online version contains supplementary material available at https://doi.org/10.1007/s10544-022-00636-w.

Funding Research supported by the National Institute of Health T32 GM135141, the National Science Foundation Grant Number 2053149, Exploratory Research Seed Grant from the Office of the Vice Chancellor for Research and Innovation, and Rutgers University School of Engineering.

Declarations

Conflicts of Interest The authors declare that they have no conflict of interest.

References

A.U. Alam, D. Clyne, H. Jin, N.-X. Hu, M.J. Deen, ACS Sens. **5**, 412 (2020)
T. Antal, M. Droz, G. Györgyi, Z. Rácz, Phys. Rev. Lett. **87**, 240601 (2001)
B.K. Ashley, M.S. Brown, Y. Park, S. Kuan, A. Koh, Biosens. Bioelectron. **132**, 343 (2019)
B.K. Ashley, U. Hassan, Wires Nanomed. Nanobiotechnol. **13**, e1701 (2021a)
B.K. Ashley, U. Hassan, Biotechnol. Bioeng. **118**, 4428 (2021b)
B.K. Ashley, U. Hassan, in 2021 43rd Annual International Conference of the IEEE Engineering in Medicine Biology Society (EMBC) pp. 1201–1204 (2021c)
B.K. Ashley, I. Mukerji, U. Hassan, in 2021 43rd Annual International Conference of the IEEE Engineering in Medicine Biology Society (EMBC) pp. 7233–7236 (2021)
A.K. Atakan, W.E. Blass, D.E. Jennings, Appl Spectrosc **34**, 369 (1980)
G. Bianchi, R. Sorrentino, Electronic Filter Simulation & Design. (McGraw Hill Professional, 2007)
A.R.C. Bredar, A.L. Chown, A.R. Burton, B.H. Farnum, A.C.S. Appl, Energy Mater. **3**, 66 (2020)
M.S. Brown, B. Ashley, A. Koh, Front. Bioeng. Biotechnol. **6**, (2018)
I.-H. Cho, J. Irudayaraj, Int. J. Food Microbiol. **164**, 70 (2013)
V.S. Chouhan, S.S. Mehta, in 2007 International Conference on Computing: Theory and Applications (ICCTA'07) pp. 512–515 (2007)
S. Cinti, M. Basso, D. Moscone, F. Arduini, Anal. Chim. Acta **960**, 123 (2017)
C.H. Clausen, M. Dimaki, C.V. Bertelsen, G.E. Skands, R. Rodriguez-Trujillo, J.D. Thomsen, W.E. Svendsen, Sensors (Basel) **18**, (2018)
B.C. Colson, A.P.M. Michel, ACS Sens. **6**, 238 (2021)
W. Gao, S. Emaminejad, H.Y.Y. Nyein, S. Challa, K. Chen, A. Peck, H.M. Fahad, H. Ota, H. Shiraki, D. Kiriya, D.-H. Lien, G.A. Brooks, R.W. Davis, A. Javey, Nature **529**, 509 (2016)
V. Gnyawali, E.M. Strohm, J.-Z. Wang, S.S.H. Tsai, M.C. Kolios, Sci. Rep. **9**, 1585 (2019)

S.-M. Han, J.-H. Cho, I.-H. Cho, E.-H. Paek, H.-B. Oh, B.-S. Kim, C. Ryu, K. Lee, Y.-K. Kim, S.-H. Paek, Anal. Chim. Acta **587**, 1 (2007)
U. Hassan, T. Ghonge Jr., B.R., M. Patel, M. Rappleye, I. Taneja, A. Tanna, R. Healey, N. Manusry, Z. Price, T. Jensen, J. Berger, A. Hasnain, E. Flaugher, S. Liu, B. Davis, J. Kumar, K. White, R. Bashir, Nat. Commun. **8**, 15949 (2017)
U. Hassan, B. Reddy, G. Damhorst, O. Sonoiki, T. Ghonge, C. Yang, R. Bashir, Technology **03**, 201 (2015)
D. Holmes, H. Morgan, N.G. Green, Biosens. Bioelectron. **21**, 1621 (2006)
R. Hu, T. Liu, X.-B. Zhang, S.-Y. Huan, C. Wu, T. Fu, W. Tan, Anal. Chem. **86**, 5009 (2014)
Z. Izadi, M. Sheikh-Zeinoddin, A.A. Ensafi, S. Soleimanian-Zad, Biosens. Bioelectron. **80**, 582 (2016)
F. Khateib, A. Mehaney, R.M. Amin, A.H. Aly, Phys. Scr. **95**, 075704 (2020)
A. Koh, D. Kang, Y. Xue, S. Lee, R.M. Pielak, J. Kim, T. Hwang, S. Min, A. Banks, P. Bastien, M.C. Manco, L. Wang, K.R. Ammann, K.-I. Jang, P. Won, S. Han, R. Ghaffari, U. Paik, M.J. Slepian, G. Balooch, Y. Huang, J.A. Rogers, Sci. Transl. Med. **8**, 366ra165 (2016)
X. Liu, L. Li, A.J. Mason, Philosophical Transactions of the Royal Society A: Mathematical. Phys. Eng. Sci. **372**, 20130107 (2014)
Y. Lu, D. Macias, Z.S. Dean, N.R. Kreger, P.K. Wong*, IEEE Trans. NanoBiosci. **14**, 811 (2015a)
Z. Lu, H. Wang, S.R. Naqvi, H. Fu, Y. Zhao, H. Song, J.B. Christen, in 2015 28th IEEE International System-on-Chip Conference (SOCC) pp. 240–244 (2015b)
T. Maetzig, J. Ruschmann, C.K. Lai, M. Ngom, S. Imren, P. Rosten, G.L. Norddahl, N. von Krosigk, L. Sanchez Milde, C. May, A. Selich, M. Rothe, I. Dhillon, A. Schambach, R.K. Humphries, Mol. Ther. **25**, 606 (2017)
M.S. Manikandan, K.P. Soman, Biomed. Signal Process. Control **7**, 118 (2012)
M.B. Marinov, G.T. Nikolov, B. Ganev, in 2018 IX National Conference with International Participation (ELECTRONICA) pp. 1–4 (2018)
R.C. Murdock, K.M. Gallegos, J.A. Hagen, N. Kelley-Loughnane, A.A. Weiss, I. Papautsky, Lab Chip **17**, 332 (2017)
K.M. Pierce, B.A. Parsons, R.E. Synovec, in Data Handling in Science and Technology, ed. By A.M. de la Peña, H.C. Goicoechea, G.M. Escandar, and A.C. Olivieri (Elsevier, 2015), pp. 427–463
M.R. Ram, K.V. Madhav, E.H. Krishna, N.R. Komalla, K.A. Reddy, IEEE Trans. Instrum. Meas. **61**, 1445 (2012)
G.G. Redhyka, D. Setiawan, D. Soetraprawata, in 2015 International Conference on Automation, Cognitive Science, Optics, Micro Electro-Mechanical System, and Information Technology (ICACOMIT) pp. 72–77 (2015)
K. Ridgway, S.P.D. Lalljie, R.M. Smith, J. Chromatogr. A **1153**, 36 (2007)
M. Sarimollaoglu, D.A. Nedosekin, Y.A. Menyaev, M.A. Juratli, V.P. Zharov, Photoacoustics **2**, 1 (2014)
Y. Singh, S. Tripathi, M. Pandey, International Journal of Computer Applications **10**, 23 (2010)
D.D. Stupin, S.V. Koniakhin, N.A. Verlov, M.V. Dubina, Phys. Rev. Applied **7**, 054024 (2017)
L.L. Sun, Y.S. Leo, X. Zhou, W. Ng, T.I. Wong, J. Deng, Materials Science for Energy Technologies **3**, 274 (2020)
T. Sun, D. Holmes, S. Gawad, N.G. Green, H. Morgan, Lab Chip **7**, 1034 (2007)
F.J. Taylor, A. Williams, Electronic Filter Design Handbook, 4th edn. (McGraw-Hill Education, 2006)
N. Verma, M. Singh, Biosens. Bioelectron. **18**, 1219 (2003)
F. Volpetti, J. Garcia-Cordero, S.J. Maerkl, PLoS ONE **10**, e0117744 (2015)
K. Wagner, M.A. Sami, C. Norton, J. McCoy, U. Hassan, RSC Adv. **11**, 21315 (2021)
L. Weinberg, P. Slepian, IRE Transactions on Circuit Theory **7**, 88 (1960)
H. Yoo, J. Shin, J. Sim, H. Cho, S. Hong, Biosens. Bioelectron. **168**, 112561 (2020)
S. Zhang, Z. Li, Q. Wei, Nanotechnology and Precision Engineering **3**, 32 (2020)
J. Zhong, M. Liang, Y. Ai, Lab Chip **21**, 2869 (2021)